

The uppermost transparent layer comprises Holocene lacustrine diatomaceous mud. It is thickest in the eastern, deepest part of the lake and thins gradually to the west, where there are extensive outcrops of the underlying sediments (Fig. 3). Five of the seven cores that we recovered from the lake penetrated the entire Holocene sequence and sampled a soil horizon. This horizon is clearly defined by profiles of magnetic susceptibility (Fig. 4) and water content in the cores, the presence of vertically oriented rootlets, and prismatic cracking characteristic of vertisols. Similar features have been described from Lake Victoria cores, but their locations were restricted to shallower water in the northern margin of the lake (9, 15).

Our deepest core, V95-2P, recovered from a depth of ~67 m (Fig. 1), clearly shows the soil horizon with vertical rootlets at the depth where the porosity drops to 50%. Pollen is poorly preserved in the vertisol and is derived mostly from grasses. The Holocene sediment immediately overlying the vertisol, representing the earliest stage of the new lake, is dominated by *typha* (cattail) pollen. [We recovered a core in May 1996 from the deepest site in the lake (68 m), midway between sites V95-2P and V95-3P depicted in Fig. 1, and again recovered vertisol at the base of unit A.] This deepest part of the lake is not separated from the major inflowing rivers by any ridge that would pond water in another part of the basin. If this site was dry, then the entire lake basin was dry, at least on a seasonal basis. This conclusion is supported by our seismic reflection profiles, which show that the hard reflector is present everywhere beneath the Holocene diatom muds. An accelerator mass spectrometer (AMS) radiocarbon date on plant macrofossils taken from just above the soil horizon at site V95-2P indicates an age of  $12,400 \pm 70$   $^{14}\text{C}$  years B.P. (Fig. 4). This age marks the onset of flooding of the lake basin at this site.

The lake level fell at ~17,300  $^{14}\text{C}$  years B.P. (9). If the deepest part of the lake basin was desiccated for several thousand years during the late Pleistocene, there would have been no lake-derived moisture, which contributes nearly 50% of the rainfall in the region today (16). Under these circumstances, satellite lakes could not have existed within the Victoria basin at that time. This result negates the possibility that the hundreds of endemic species of fish in modern Lake Victoria found adequate refuge during the arid period to maintain the diversity that they exhibit today. The alternative is that most of these species have evolved during the past 12,400 years. This conclusion is supported by evidence for the rapid speciation of cichlids in Lake Malawi (17) and by mitochondrial DNA

evidence that the Lake Victoria species flock is young, certainly less than 200,000 years old and perhaps as young as 14,000 years, and is monophyletic or derived from a single ancestral species (18). Our results indicate that this evolution occurred in the past 12,000 years. The rich diversity of Lake Victoria cichlids is clearly associated with lacustrine instability, not with an ecosystem that has been well buffered from environmental disturbance.

#### REFERENCES AND NOTES

1. P. H. Greenwood, *Bull. Br. Mus. Nat. Hist. Zool.* **39**, 1 (1980); L. Kaufman and P. Ochumba, *Conserv. Biol.* **7**, 719 (1993).
2. A. R. McCune, K. S. Thomson, P. E. Olsen, in *Evolution of Fish Species Flocks*, A. A. Echelle and I. Kornfield, Eds. (Univ. of Maine Press, Orono, ME, 1984), pp. 27–44.
3. A. Meyer *et al.*, *Nature* **347**, 550 (1990); A. Meyer, T. D. Kocher, A. C. Wilson, *ibid.* **350**, 467 (1991).
4. W. W. Bishop and A. F. Trendall, *Q. J. Geol. Soc. London* **122**, 385 (1967).
5. J. C. Doornkamp and P. H. Temple, *Geogr. J.* **132**, 238 (1966).
6. W. W. Bishop and M. Posnansky, *Uganda J.* **24**, 44 (1966).
7. P. E. Kent, *Geogr. J.* **100**, 22 (1944).
8. K. J. Sene and D. T. Plinston, *Hydro. Sci. J.* **39**, 47 (1994).
9. M. R. Talbot and D. A. Livingstone, *Palaeogeogr. Palaeoclimatol. Palaeoecol.* **70**, 121 (1989).
10. The seismic system included a 16.4-cm<sup>3</sup> air gun for the seismic source and a 10-element, single-channel, towed array for the reception of reflected signals. Single-channel data were digitally acquired aboard the research vessel (R.V.) *Ibis* at a speed of 8 to 10 km/hour. Navigational fixes were obtained every 10 s by an autonomous global positioning system. Subsequent data processing involved application of a bandpass filter (60 to 500 Hz), three-trace moving average horizontal stack, 100-ms automatic gain control window, time-variant filter, and 10:1 trace compression to achieve the clearest display of the subbottom geology.
11. C. A. Scholz *et al.*, *J. Afr. Earth Sci.* **11**, 25 (1990).
12. Depositional sequences in seismic records are defined on the basis of basal unconformities, which are usually observed in basin margin settings. These sequence boundaries typically can be traced into deeper basin settings as correlative conformable reflections (13).
13. P. R. Vail *et al.*, *Am. Assoc. Pet. Geol. Mem.* **26**, 49 (1977).
14. C. S. Feibel and F. H. Brown, *J. Hum. Evol.* **21**, 221 (1991).
15. J. C. Stager, P. N. Reinthal, D. A. Livingstone, *Freshwater Biol.* **15**, 15 (1986).
16. H. Flohn and T. Burkhardt, *Z. Gletscherk. Glazialgeol.* **21**, 125 (1985).
17. R. B. Owen *et al.*, *Proc. R. Soc. London Ser. B* **240**, 519 (1990).
18. A. Meyer, C. M. Montero, A. Spreinat, in *The Limnology, Climatology and Paleoclimatology of the East African Lakes*, T. C. Johnson and E. Odada, Eds. (Gordon and Breach, Newark, NJ, 1996), pp. 303–324.
19. We thank P. Cattaneo, J. Lapuken, D. Verschuren, T. Holst, T. Laerdal, H. Malinga, A. Byakagaba, and the captain and crew of the R.V. *Ibis* for their able assistance on Lake Victoria. L. Kaufman and A. Meyer reviewed earlier drafts of the manuscript. The Fisheries Research Institute of Jinja, Uganda, provided logistical support and access to the R.V. *Ibis*. We appreciate permission granted by the governments of Uganda and Tanzania to undertake this research. Financial support was provided to IDEAL by NSF and the Norwegian Research Council.

8 May 1996; accepted 18 June 1996

## Simultaneous Measurement of Local Gain and Electron Density in X-ray Lasers

R. Cauble,\* L. B. Da Silva, T. W. Barbee Jr., P. Celliers, C. Decker, R. A. London, J. C. Moreno, J. E. Trebes, A. S. Wan, F. Weber

X-ray lasers (XRLs) have experimental average gains that are significantly less than calculated values and a persistently low level of spatial coherence. An XRL has been used both as an injected signal to a short XRL amplifier and as an interferometer beam to measure two-dimensional local gain and density profiles of the XRL plasma with a resolution near 1 micrometer. The measured local gain is in agreement with atomic models but is unexpectedly spatially inhomogeneous. This inhomogeneity is responsible for the low level of spatial coherence observed and helps explain the disparity between observed and simulated gains.

Since the first demonstration of a collisionally excited laboratory-produced XRL in 1985 (1), much effort has been devoted toward understanding the production of the laser and enhancing the features that make XRLs powerful laboratory tools (2, 3). The

gain medium for the XRL is a plasma created by the heating of a target foil with an intense optical laser focused into a line along which amplification occurs. Atoms in the target plasma are ionized to a long-lived state, such as a neon-like state, and electron collisions within the plasma excite the upper lasing level, which spontaneously decays, emitting a photon at the laser wavelength  $\lambda$ . Amplification continues for as

Lawrence Livermore National Laboratory, University of California, Livermore, CA 94550, USA.

\*To whom correspondence should be addressed.

long (45 to 200 ps) as the appropriate plasma conditions persist, which is governed by the optical driving laser. Generally, the longer the line plasma, the greater the amplification but also the larger the probability that lasing photons will leave the plasma as a result of gradients in the medium. If a target foil a few centimeters long is used, the resulting XRL is highly monochromatic ( $\lambda/\Delta\lambda \sim 10000$ ), has a short wavelength (35 to 300 Å), has a short pulse duration, and has substantial power (kilo- to megawatts) and brightness. The XRL also has sufficient longitudinal coherence for phase-based applications.

These features make XRLs valuable in probing applications. XRLs can make efficient use of multilayer mirror technology and thus can be used in imaging systems. An XRL can be used to perform x-ray microscopy and holography of biological specimens (4). As plasma probes, XRLs have been used to perform deflectometry (5), radiography (6, 7), and interferometry (8, 9) on large ( $\sim 1$  mm) dense plasmas relevant to inertial confinement fusion (10) and laboratory astrophysics (11). These plasmas are inaccessible to optical or ultraviolet probes because of absorption and refraction and to nonlaser x-ray probes that lack such resolution and brightness.

Despite extensive efforts, model simulations overestimate the observed gain and spatial coherence properties. Additionally, research has been directed toward enhancing XRL brightness and coherence (12). Enhanced brightness has been achieved through improved target and experimental design, but the XRL remains spatially incoherent.

Predictions of XRL performance start with a calculation of the local laser gain found from an atomic model with level populations determined by expected conditions in the XRL plasma. For the neon-like yttrium XRL that we investigated here, where the expected plasma electron density

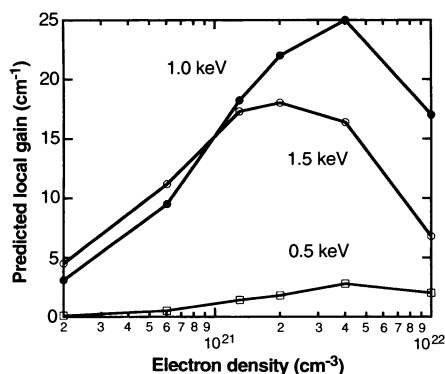


**Fig. 1.** Plot of predicted local gain of the 155 Å, neon-like yttrium lasing line versus electron density and electron temperature.

is  $\sim 10^{21}$  cm<sup>-3</sup> and the temperature is near 1 keV, the calculated local gain is in the range of 10 to 20 cm<sup>-1</sup> (Fig. 1). Laser line trapping and radiation propagation with refraction, accounted for in full two-dimensional (2D), time-dependent hydrodynamic simulations, lower the average calculated gain to 10 to 11 cm<sup>-1</sup> for XRLs a few centimeters in length (13). However, the average measured gain for the yttrium laser is still lower,  $\sim 5.3$  cm<sup>-1</sup> (14). Similar results have been found for other neon-like XRLs such as germanium (15) and selenium (16): the best modeled gain predictions are 1.5 to 2 times the measured average gain.

One source of uncertainty has been the accuracy of the atomic kinetics calculations. We used the XRL beam from a long (3-cm) target to probe a short (2-mm) XRL target that was driven in the same manner as the longer target. The short target acted as a one-pass amplifier of the incident probe from which the gain in the amplifier could be measured (17). Because the amplifier was so short, there was negligible refraction of the lasing line. By using a highly collimated incident beam, we were able to minimize transverse averaging of the local gain. The measurements allowed us to obtain the local gain profile with very high spatial resolution (1.3 μm). We also performed the gain measurements with an interferometer that uses the XRL so that we could simultaneously measure the electron density profile. Both experimental features are necessary if we are to determine why measured XRL gain and coherence fall below predictions.

The XRL we investigated is a 3p-to-3s transition in neon-like yttrium at 155 Å (14, 18). The probe XRL is produced by irradiating a 3-cm-long target (210 nm of yttrium deposited on a 100-nm Lexan substrate) with one beam of the Nova laser ( $\lambda_L = 0.53$  μm) in a 120-μm-wide line focus for

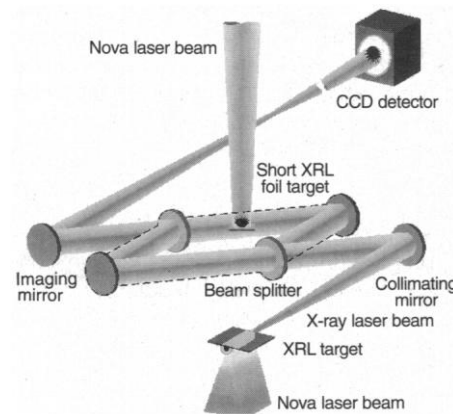


**Fig. 2.** Experimental setup for XRL interferometry of laser plasma targets. In these experiments, the upper target is the short yttrium or selenium foil to be examined.

600 ps at an intensity of  $1.5 \times 10^{14}$  W cm<sup>-2</sup>. The XRL, which lasts about 75 ps, is generated and amplified in the resulting plasma.

To measure the gain, we used an assembly of multilayer optical components to provide a narrow bandpass system ( $155 \pm 4$  Å) to reduce noise from plasma emission and a high magnification (19× with a spatial resolution of 1.3 μm) (Fig. 2). Multilayer beam splitters were used to create a Mach-Zehnder 155 Å interferometer, which was used to measure the 2D electron density profile of the amplifier. The signal was recorded on a 1024 element by 1024 element charge-coupled device (CCD) camera; the short ( $\sim 75$  ps) duration of the XRL pulse effectively gated the image. Additional filters around the CCD eliminated stray optical light. While the XRL target was driven with one beam of Nova, the amplifier was driven with another line-focused Nova beam time-delayed for arrival of the XRL beam.

To provide a comparison with the yttrium amplifiers, we imaged 2-mm-long selenium exploding foils (80 nm on 100-nm Lexan), which provide no amplification, in the interferometer. An interferogram of a selenium foil is shown in Fig. 3. The view is end-on, with the yttrium XRL backlighting the selenium foil; the foil lies horizontally located at zero on the vertical scale. The Nova laser beam is incident from above with the line focus along the line of sight (out of the page). The image was taken midway into the drive pulse. The light areas are self-emission near the wings of the Nova beam; although selenium is itself an XRL, the lasing wavelengths (206 and 209 Å) are outside the bandpass of the imaging system and do not appear in the image. The num-

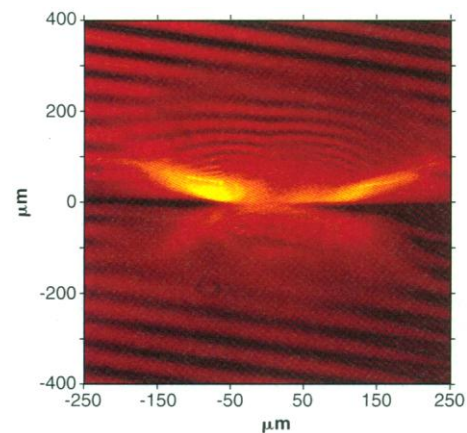


**Fig. 3.** An interferogram at 155 Å of a 2-mm-long selenium foil driven from above by one Nova laser beam (120 μm full width at half maximum). The image was taken midway through the driving pulse. The maximum intensity is 1000 counts per pixel above background.

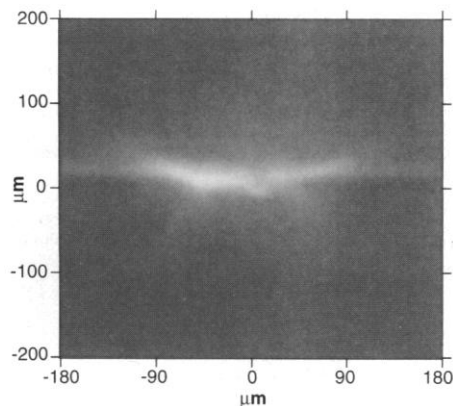


**Fig. 4.** Image of the self-emission of a 2-mm-long yttrium foil driven by a Nova line-focus laser beam. There is no XRL backlighter. The maximum intensity is 600 counts per pixel above background.

ber of counts per pixel in the emission regions is  $\sim 1000$  above background.

Parallel fringes at the top and bottom of the image are regions of zero density. A finite electron density causes a shift in the fringe spacing from which the product  $n_e L$ , where  $n_e$  is the electron density and  $L$  is the probe path length, can be found (8); a shift of one fringe corresponds to a density of  $3.5 \times 10^{19} \text{ cm}^{-3}$  for  $L = 2 \text{ mm}$ . Blurred areas near  $225 \mu\text{m}$  above and  $150 \mu\text{m}$  below the foil are smearing caused by plasma that is moving too fast for the 75-ps exposure time. Interior to these areas are regions of good fringe visibility with a peak electron density of  $5 \times 10^{20} \text{ cm}^{-3}$  near the center of the foil. The interferogram shows bilobed ablation possibly due to a small ( $\sim 5\%$ ) anomaly in the Nova beam; this feature did

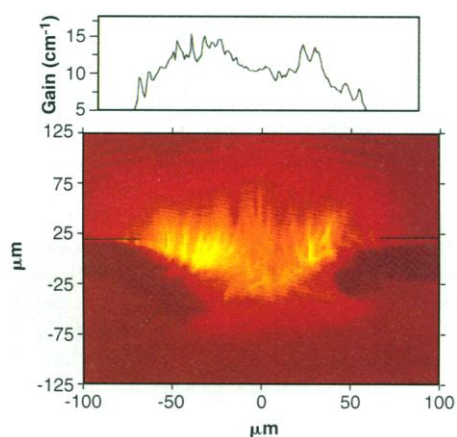


**Fig. 5.** Interferogram of a 2-mm-long yttrium foil driven by a Nova line-focus laser beam (from above). The light regions are areas of intense local amplification of the backlighting yttrium XRL. The maximum intensity is 40,000 counts per pixel above background. The plot is local gain along a horizontal line indicated on the image. The position of the line is indicated by the bars on either side of the image.

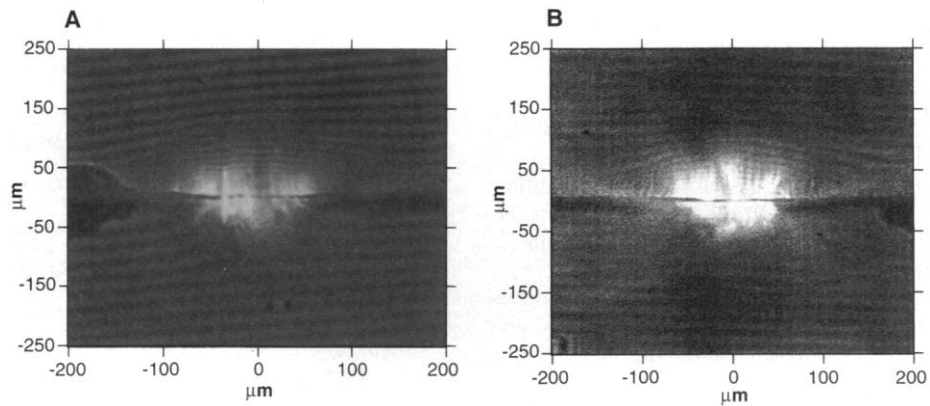


**Fig. 6. (A and B)** Two interferograms of short yttrium foils driven (from above) by a Nova line-focus laser beam. As in Fig. 5, there are regions of high local amplification. These images are partially saturated as a result of high gain.

not appear on subsequent shots.

In order to examine self-emission of an yttrium target, we used a 2-mm yttrium foil that was irradiated but not probed by an XRL beam (Fig. 4). As in Fig. 3, the foil, sitting at zero on the vertical scale, is irradiated from above by a  $120\text{-}\mu\text{m}$  line focus along the line of sight. All that is visible is unstructured emission. The maximum number of counts per pixel is  $\sim 600$  above the background.

An image of an yttrium foil the same length as the one in Fig. 4 under the same drive conditions is shown in Fig. 5, except that the foil is backlit by an yttrium XRL so that the foil plasma acts as an XRL amplifier. The data show strong amplification; the number of counts throughout most of the plasma is 10,000 to 40,000 above background. The local gain can be found from  $I = I_0 e^{gL} + I_0 + I_S$ , where  $I$  is the amplified intensity,  $I_0$  the incident intensity (equal to one-half the recorded background because the background is delivered through two arms of the interferometer),  $I_S$  the self-emission value taken from Fig. 3,  $g$  is the gain, and  $L$  is the amplification path length (2 mm). The local gain is 10 to  $15 \text{ cm}^{-1}$  in the central plasma, in general agreement with atomic models. A plot of local gain along a horizontal line indicated in the image is displayed in Fig. 5. The area of significant gain is limited to  $\sim 125 \mu\text{m}$  across the spot (horizontally) and from  $\sim -50 \mu\text{m}$  to  $\sim +125 \mu\text{m}$  vertically.

Although the average local gain is about  $10 \text{ cm}^{-1}$ , it is clearly not homogeneous. There are pockets of dimension 5 to  $10 \mu\text{m}$  where the local gain is higher (as high as  $18 \text{ cm}^{-1}$ ). This structure is repeatable: small regions of more intense gain were observed in all yttrium amplifier shots, although the location and number of such regions varied. Figure 6, A and B, shows two interferograms of yttrium foils similar to that in Fig. 5. Although we

cannot quantify the gain for the shots in Fig. 6 because the CCD was saturated, small, high-gain areas are evident. We infer that the gain medium, in which the propagation and amplification of the XRL beam are quite complicated, is highly non-uniform. This result is unexpected, and simulations of XRLs have not included this structure.

In addition, the local gain is higher near the edges of the beam spot (left and right of center in the images). These are regions of higher density gradients. Stronger gradients and proximity to the plasma boundary make it more likely that laser light that originates near the edges is refracted out of the line plasma in a long XRL. Hydrodynamic simulations predict higher densities but also lower temperatures near the edges, resulting in lower calculated gain in the wings of the plasma; the images show that the opposite is true.

The actual cause of the small-scale structure in the local gain is unknown, but we believe that it is the result of temperature fluctuations in the plasma. In Fig. 6, there are density variations in the vicinity of the high-gain regions, but slight shifts in the fringes correspond to variations of only 10 to 20% across the regions, whereas somewhat larger variations are necessary to significantly affect gain (Fig. 1). This leaves the electron temperature as the parameter most likely to affect the gain.

We believe that these temperature fluctuations are due to nonuniformities in the driving beam. Intensity modulations in the line focus may tend to be arranged along the line focus, creating thin "stripes" of higher (or lower) intensity that could act as channels of higher amplification embedded in a smoother, lower gain background. As long as the driving beam is static over the time of peak gain, such channels might not dissipate during the amplifying interval ( $\sim 75 \text{ ps}$ ). This dissi-

pation is difficult to calculate because electron conduction from simulated hot spots is very fast, dissipating the high temperature on time scales that are short compared to 75 ps. We have assumed that these channels run the full 2-mm length of the target. There is no way to determine if this is actually the case; if the regions are less than 2 mm, then the local gain in those regions will be even higher.

Although laser-plasma instabilities, such as thermal self-focusing, can also give rise to small-scale filaments of high-temperature plasma, this is an unlikely cause of the observed structure because not only does filamentation tend to drive the density down in small filaments and thus, according to Fig. 1, toward regimes of lower gain, but also we do not observe the density fluctuations associated with this mechanism. Hydrodynamic instabilities, such as Rayleigh-Taylor, seem unlikely for the same reason: the density variation is not observed.

It is possible that the ion temperature  $T_i$ , not the electron temperature, is the cause of the regions of high local gain. Because the lasing line narrows as  $T_i$  decreases, the resulting gain varies as  $T_i^{-1/2}$ . Small regions of lower  $T_i$ , possibly seeded by fluctuations in the driving laser, would be areas of enhanced gain.

The nonuniform structure has a significant effect on XRL coherence. An XRL of this type behaves like an incoherent source over the output aperture of the XRL (19, 20). This persistent lack of coherence has not been understood; one suggested explanation is the development of plasma instabilities, seeded by intensity modulations in the driving laser, which break up the plasma (21).

As we have observed from Figs. 5 and 6, the region of amplification in the XRL plasma is indeed highly inhomogeneous, although probably not because of plasma instabilities. Because much of the gain is generated in small isolated regions, the spatial coherence of the XRL cannot be improved without smoothing the temperature field in the plasma. If the isolated gain structure is caused by modulations in the driving laser, smoothing of the driving beam may alleviate the pockets and improve the spatial coherence of the XRL.

## REFERENCES AND NOTES

- D. L. Matthews *et al.*, *Phys. Rev. Lett.* **54**, 110 (1985).
- R. C. Elton, *X-Ray Lasers* (Academic Press, New York, 1990).
- C. H. Skinner, *Phys. Fluids* **B3**, 2420 (1991).
- J. E. Trebes *et al.*, *Science* **238**, 517 (1987); L. B. Da Silva *et al.*, *ibid.* **258**, 269 (1992).
- D. Ress *et al.*, *ibid.* **265**, 514 (1994).
- R. Cauble *et al.*, *Phys. Rev. Lett.* **74**, 3816 (1995).
- D. H. Kalantar *et al.*, *ibid.* **76**, 3574 (1996).
- L. B. Da Silva *et al.*, *ibid.* **74**, 3991 (1995).
- A. S. Wan *et al.*, unpublished results.
- M. D. Cable *et al.*, *Phys. Rev. Lett.* **73**, 2316 (1994); L. J. Suter *et al.*, *ibid.*, p. 2328; T. R. Dittrich *et al.*, *ibid.*, p. 2324; R. L. Kauffman *et al.*, *ibid.*, p. 2320.
- T. S. Perry *et al.*, *ibid.* **67**, 3784 (1991); L. B. Da Silva *et al.*, *ibid.* **69**, 438 (1992).
- R. Kodama *et al.*, *ibid.* **73**, 3215 (1994); C. L. S. Lewis *et al.*, *Opt. Commun.* **91**, 71 (1992); P. Jaegle, *Phys. Today* **48**, 109 (April 1995).
- R. Ratkowsky *et al.*, in *1994 Inertial Confinement Fusion Annual Report, UCRL-LR-105820-94* (available from the National Technical Information Service, 5285 Port Royal Road, Springfield, VA 22161), p. 63.
- G. M. Shimkaveg *et al.*, *Proc. Soc. Photo-Opt. Instrum. Eng.* **1551**, 84 (1992).
- A. S. Wan *et al.*, *Opt. Eng.* **33**, 2434 (1994).
- B. J. MacGowan *et al.*, *Phys. Fluids* **36**, 2326 (1992).
- C. H. Skinner, *Opt. Lett.* **16**, 1266 (1991).
- L. B. Da Silva *et al.*, *ibid.* **18**, 1174 (1993).
- J. E. Trebes *et al.*, *Phys. Rev. Lett.* **68**, 588 (1992).
- P. Celliers *et al.*, *Opt. Lett.* **20**, 1907 (1995).
- P. Amendt, M. Strauss, R. A. London, *Phys. Rev. A* **53**, R23 (1996).
- This work was performed under the auspices of the Department of Energy by Lawrence Livermore National Laboratory under contract W-7405-ENG-48.

22 April 1996; accepted 24 June 1996

## BTK as a Mediator of Radiation-Induced Apoptosis in DT-40 Lymphoma B Cells

Fatih M. Uckun,\* Kevin G. Waddick, Sandeep Mahajan, Xiao Jun, Minoru Takata, Joseph Bolen, Tomohiro Kurosaki

Bruton's tyrosine kinase (BTK) is a member of the SRC-related TEC family of protein tyrosine kinases (PTKs). DT-40 lymphoma B cells, rendered BTK-deficient through targeted disruption of the *btk* gene by homologous recombination knockout, did not undergo radiation-induced apoptosis, but cells with disrupted *lyn* or *syk* genes did. Introduction of the wild-type, or a SRC homology 2 domain or a pleckstrin homology domain mutant (but not a kinase domain mutant), human *btk* gene into BTK-deficient cells restored the apoptotic response to radiation. Thus, BTK is the PTK responsible for triggering radiation-induced apoptosis of lymphoma B cells, and its kinase domain is indispensable for the apoptotic response.

Apoptosis, also termed programmed cell death, is a common mode of eukaryotic cell death characterized by distinct ultrastructural features and a ladder-like DNA fragmentation pattern produced by endonuclease-mediated cleavage of DNA into oligonucleosome-length fragments (1). Apoptosis plays an important role in the development and maintenance of a functional immune system (1). A better understanding of the biochemical events leading to apoptosis may provide further insights into the pathogenesis and treatment of human diseases, such as immunodeficiencies, autoimmune disorders, leukemias, and lymphomas, which are thought to stem from inherited or acquired deficiencies of checkpoints regulating the rate of apoptosis in lymphoid cells.

Reactive oxygen intermediates have been implicated as mediators of apoptosis in B-lineage lymphoid cells (1, 2). The molecular mechanism by which reactive oxygen intermediates can trigger apoptosis has not yet been deciphered, but it may involve

activation of as yet unidentified protein tyrosine kinases (PTKs) (2). Protein tyrosine kinases play a pivotal role in the initiation of biochemical signaling events that affect proliferation, differentiation, and survival of B-lineage lymphoid cells (3-7). In addition to radiation-induced apoptosis (2), other apoptotic death signals, including those induced by dexamethasone, monoclonal antibodies to CD3, tumor necrosis factor- $\alpha$ , ceramide, FAS ligand, and Taxol, are triggered by enhanced PTK activity (8).

DT-40 is a radiation-sensitive chicken lymphoma B cell line that we have previously used to explore the mechanisms whereby various PTKs that participate in B cell antigen receptor signaling (9-11). DT-40 cells undergo rapid apoptosis after exposure to  $\gamma$ -rays, as measured by a quantitative flow cytometric apoptosis-detection assay (2, 12-14). Radiation-induced apoptosis of DT-40 cells is triggered by activation of radiation-responsive PTKs because it is prevented by the PTK inhibitor genistein (2, 12-14). One of the radiation-responsive PTKs in DT-40 cells is the 77-kD TEC PTK family member Bruton's tyrosine kinase (BTK) (4, 15-20). We now provide experimental evidence that the BTK tyrosine kinase, but not the LYN, SYK, or CSK tyrosine kinases, mediates radiation-induced apoptosis of DT-40 lymphoma B cells. BTK is also responsible for mediating

F. M. Uckun, K. G. Waddick, S. Mahajan, X. Jun, Molecular Signal Transduction Laboratory, Biotherapy Institute, University of Minnesota, Roseville, MN 55113, USA. M. Takata and T. Kurosaki, Section of Immunobiology, Yale University School of Medicine, New Haven, CT 06510, USA. J. Bolen, DNAX Research Institute of Molecular and Cellular Biology, Palo Alto, CA 94304, USA.

\* To whom correspondence should be addressed.